I^2SIM: Boosting High-Fidelity Isotropic Super-Resolution with Image Interference and Spatial-Spectrum Optimization

Enxing He[1], Yile Sun[1], Hongfei Zhu[2], Xinxun Yang[1], Lu Yin[3], Yubing Han[1*], Cuifang Kang[1,4,5*], Xu Liu[1,4,5]

[1*]State Key Laboratory of Extreme Photonics and Instrumentation, College of Optical Science and Engineering, Zhejiang University, Hangzhou, 310027, Zhejiang, China.
[2]Department of Biomedical Engineering, The Chinese University of Hong Kong, Hong Kong, China.
[3]College of Optical and Electronic Technology, China Jiliang University, Hangzhou, 310018, Zhejiang, China.
[4]ZJU-Hangzhou Global Scientific and Technological Innovation Center, Hangzhou, 311200, Zhejiang, China.
[5]Collaborative Innovation Center of Extreme Optics, Shanxi University, Taiyuan, 030006, Shanxi, China.

*Corresponding author(s). E-mail(s): hanyubing@zju.edu.cn; cfkuang@zju.edu.cn;
Contributing authors: zjuenxinghe@gmail.com; yilesun@zju.edu.cn; hfzhu9927@link.cuhk.edu.hk; 22230022@zju.edu.cn; yinlu890622@163.com; liuxu@zju.edu.cn;

Abstract

Spacial resolution and temperal resolution make great sense in subcellular structures imaging. Three-dimensional structured illumination microscopy(3D-SIM) achieves a balance between them. However, its axial resolution is limited to about 300 nm. Here we report a new method by employing two oppositely positioned objectives to detect fluorescence based on three-beam structured illumination. With the aid of spectral modulation and spatial domain Frobenius Hessian optimization, the axial resolution can reach twice that of 3D-SIM,reaching

approximately 120 nm and the acquisition process remains the same as 3D-SIM. Moreover, several samples like beads, microtubules and actin filaments were tested to demonstrate the potential of our method.

Keywords: optical imaging, super-resolution microscopy, fluorescence interference, structured illumination microscopy, optimization

1 Introduction

Comprehensive observation of subcellular structures at high spatial and temporal resolutions plays a crucial role in studying biological activities. To achieve this, about three super-resolution microscopic methods have been proposed, including stimulated emission depletion microscopy(STED) [1–3], single-molecule localization microscopy(SMLM) [4–7] and structured illumination microscopy(SIM) [8–11]. At beginning, they were all used to enhance lateral resolution. However, with the increasing demand for resolving axial information, 3D-STED introduced an axial illumination pattern [12, 13], 3D-SMLM utilized point spread function(PSF) engineering to encode axial information [14–16], and 3D-SIM introduced central illumination light to create variations in illumination structure along the axial direction [9]. As a result, 3D-STED and 3D-SMLM can achieve $\sim 30 - 50$ nm axial resolution at the cost of high-power density lasers and long acquisition time [17]. To strike a balance between temporal and spatial resolution, it is important to seek a method that enhances the axial resolution of 3D-SIM from 300 nm to a more advanced level.

I^5S was proposed to address this issue by employing six beams for illumination and capturing fluorescence using two objectives positioned oppositely [18, 19]. It is able to reach an axial resolution of ~ 100 nm. However, due to its intricate illumination and capturing setup, coupled with the sophisticated reconstruction process, its practical application is challenging. 4-beam SIM [20] simplified acquisition set up by using wide-field detection and put a mirror against objective to generate 4-beam illumination. It can reach a 2-fold axial resolution improvement compared to 3D-SIM but still need fine-tuning at the illumination end.

In our previous work [21], fluorescence interference structured illumination microscopy (FI-SIM) enabled an axial resolution of nearly 30 nm by employing fluorescence interference and multi-channel detection. The axial information was calculated differently from lateral reconstruction which makes the method to be used on multi-layers samples. Here we propose a method using opposite objectives to detect based on I^2M [22] and three beams to illuminate to avoid cumbersome adjustments at the illumination end. To further enhance the quality of imaging, spectral modulation and spatial domain Frobenius Hessian optimization are used to eliminate artifacts and noise which is inspired by Hessian-SIM [23, 24]. In this way, axial resolution can be extended to ~ 130 nm under 561 nm illumination laser with 3D-SIM's lateral resolution. We tested our method in beads, microtubules and actin filaments.

2 Results

2.1 Principle

The 4Pi configuration can naturally enhance the resolution in wide-field imaging because of the opposite objective setup. Through interference of fluorescence, the OTF supporting region in the k_z axis can be extended from $[1 - cos(sin^{-1}(\mathrm{NA}/n))] \cdot nk_{em}$ to $2nk_{em}$, where NA denotes the numerical aperture, n is the refractive index of the immersion medium, and k_{em} is the wave vector of fluorescence in vacuum. However, despite the extended max value, there are still low-value regions and zero-value regions in the supporting area, making the z-axis sectioning ability weak. To fill up the missing value, one way is to shift OTF supporting area and then combine them, which is exactly the operation SIM(structured illumination microscopy) does. To achieve this, we used three beams to generate illumination pattern through one objective and detect the fluorescence through 4Pi configuration as shown in Fig. 1a. On the right side of Fig. 1a, the upper row shows theoretical 4Pi PSF generated using vectorial diffraction theory which has side lobes [25] and its profile when the phase difference between two optical path through opposite objective is 0. The lower row demonstrates the 4Pi wide-field OTF and its augmented density which is calculated as $log(|\cdot| + 1)$. The center of OTF has zero points and the side has low-value points.

An important part in 4Pi-SIM is the reconstruction after obtaining raw images. Here we applied Open-3DSIM [26] as framework and adjusted it to suit 4Pi imaging. The pipeline is shown in Fig. 1b. First an image stack is collected, each layer has 15 slices corresponding to 3D-SIM. A simulated 4Pi OTF is used to replace the original wide-field OTF to build frequency domain filters. Although filters can increase resolution and surpass noise and side lobes, there still exist artifacts and noises due to the unsmooth synthetic OTF. To solve this problem, space-domain optimization using frobenius norm of Hessian and l_1 norm as regularization is applied. After the reconstruction of open3D-SIM, we can construct the following loss function:

$$\underset{f}{argmin}\{\frac{1}{2}\|Hf - b\|_2^2 + \lambda_1\|f\|_1 + \lambda_2\|Hessian_{Frob}(f)\|_1\} \tag{1}$$

f is the SIM result with artifacts. The operator H in loss function is a binary frequency mask which shares the same region as reconstructed 4Pi-SIM OTF to make sure the fidelity is considered only in physically detected area. $\|\cdot\|_1$ and $\|\cdot\|_2$ are l_1 and l_2 norms, respectively. l_1 norm guarantees the sparsity and frobenius norm of Hessian recovers the continuity of sample with better ISNR [27], respectively. The frobenius norm of Hessian can be represented as:

$$Hessian_{Frob}(f) = \sqrt{f_{xx}^2 + 2f_{xy}^2 + f_{yy}^2 + 2\lambda_z f_{xz}^2 + 2\lambda_z f_{yz}^2 + \lambda_z^2 f_{zz}^2} \tag{2}$$

Here $f_{xx} = \partial^2 f/\partial x^2$, and similar operations are performed for the others. λ_1, λ_2, and λ_z adjust the weights of various terms, balancing fidelity and regularization. By optimizing the loss function using Alternating Direction Method of Multipliers(ADMM) iteratively which will be further discussed in Methods, the recovered OTF will have

a more uniformly extended supporting region than 3D-SIM as shown in Fig. 1c. The performance of algorithm will be discussed in next section.

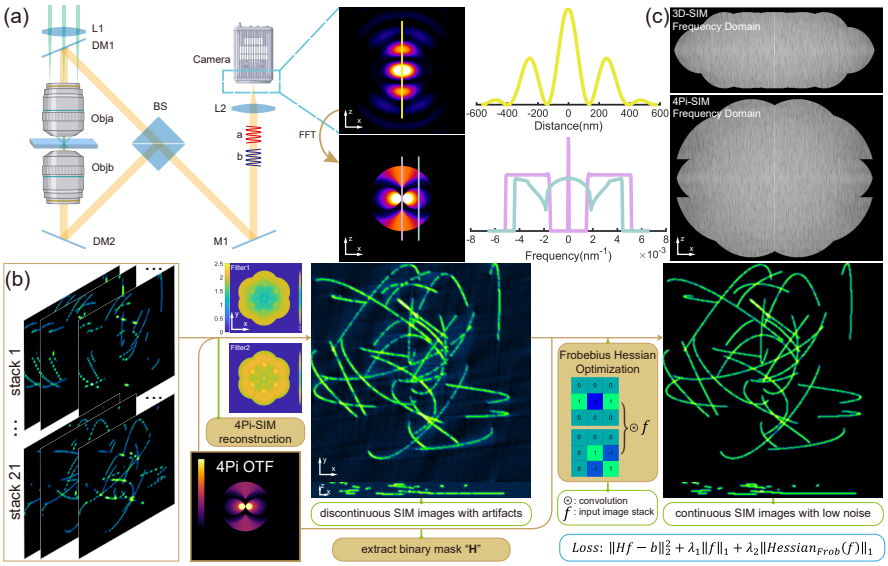

Fig. 1 Principle of 4Pi-SIM. (a)(Left)Structure schematic diagram of 4Pi-SIM. The sample is illuminated by three beams the same as 3D-SIM through one objective and fluorescence detected by both objectives will interfere with each other on CMOS; (Middle)4Pi PSF on CMOS and its OTF. Line profile of PSF is normalized and Profiles of OTF were calculated by normalized $log(abs(Intensity)+1)$; (Right)Profiles corresponding to Middle. (b)Algorithm flow. (c)Comparison of OTF supporting region between 3D-SIM and 4Pi-SIM.

2.2 Simulation and Calibration

Simulated randomly three-dimensionally distributed beads and microtubules were used to verify the effectiveness of the method. Beads sample was generated as points of no diameter and then convolved by wide-field PSF and 4Pi PSF with 0 phase difference. Because of 0 nm diameter, the reconstructed result can reflect real resolution. The PSF was generated using the method mentioned before with 1.45 NA objective and 1.518 refractive index. The pixel size in x-y plane was 83.6 nm and 50 nm in z axis. After reconstruction, x-y pixel size was interpolated to 41.8 nm and z axis was not interpolated. The axial range was from -800 nm to 800 nm which means there were 31 layers. Result is shown in Fig. 2a, our method shared same lateral resolution with 3D-SIM. The axial resolution between wide-field, open3D-SIM and our method was compared on the right side of Fig. 2a, axial diameter was dramatically decreased and OTF supporting area's max value was extended from $\sim 1.4k_{em}$ to $\sim 2.7k_{em}$. The full-width at half-maximum(FWHM) values for wide-field, open3D-SIM, and our method are 497.1 nm, 284.4 nm and 133.0 nm under center emission wavelength of 590 nm, respectively. Microtubules with the same pixel size and wavelength of beads were also simulated to test the performance under complicated situation.The pixel number was

301 laterally and 21 axially. The upper row of Fig. 2 is a middle slice comparing three methods. It is worth noting that, although 3D-SIM and our method share the same lateral resolution, our approach exhibits fewer artifacts in each slice. This improvement is attributed to the higher axial resolution, which mitigates the influence of adjacent slices. In the bottom of Fig. 2c, one slice in x-z plane shows that our method presents clearer axial structures.

we also examined reconstruction performance on high-density 100 nm fluorescent bead sample (FluoSpheres beads, F8801) under 561 nm excitation wavelength. In the open3D-SIM reconstruction process, we set the notch depth to 0.96 for $filter_1$ and 0.98 for $filter_2$. For the optimization step, $lambda_1$ was 0.05, $lambda_2$ was 0.005, and $lambda_z$ was 1. Only one slice in x-z plane is depicted for simplicity (Fig. 2d). As expected, our method maintained the ∼2-fold lateral resolution enhancement of 3D-SIM over wide-field microscopy while offering ∼2-fold-better axial resolution than 3D-SIM. We counted 76 beads for wide-field, 100 beads for 3D-SIM, and 100 beads for 4Pi-SIM, and plotted their box plots(Fig. 2. Their average FWHM were 633.7 nm, 302.3 nm, and 178.4 nm, respectively. Taking into account the size of the beads, this result is in line with our expectations.

2.3 Cell Imaging

To verify the performance of our method in applications, we used it to test several cell samples in which the imaging condition was more complicated. Fixed microtubule networks of BSC cells were first tested(Fig. 3). 647 nm laser was used to excite the fluorophores which was labeled with the Abberior STAR Red. The 3D illumination pattern was centered at the focal plane of objective. For each layer, we took 15 images(5 phases per orientation × 3 orientation) and then moved z-piezo stage 50 nm to focus on another layer. The reason we chose a 50 nm layer interval was to comply with the Nyquist sampling theorem, given that the axial resolution is approximately 130 nm. Taking into account the thickness of the cells and the range of microtubules, the number of scanning layers was set to 21. This allows for the reconstruction of the structure of the important layers with minimal information loss while also maintaining the speed of reconstruction. By setting the exposure time for each acquisition to 35 ms, we achieved the minimum total imaging time of 12 seconds for volume imaging. However, considering the reaction of machine and the stability of the piezo stage, the total imaging time extended to 71 s.

To have the best performance of the algorithm, parameters should be carefully selected. In the open3D-SIM reconstruction process, we set the notch depth to 0.96 for $filter_1$ and 0.98 for $filter_2$ in order to achieve a balance between enhancing resolution and preserving signal integrity. For the optimization step, $lambda_1$ was 0.06, $lambda_2$ was 0.02, and $lambda_z$ was 1. Depth-encoded images revealed that microtubules were primarily concentrated in the upper layer of the photographed area. Furthermore, the enlarged view confirmed that our approach matched the lateral resolution of 3D-SIM and experienced reduced axial interference(Fig. 3a). In axial view, wide-field microscopy could barely discern the closely spaced microtubules, the intervals of which were more distinctly visible in 3D-SIM. However, by employing our method, structures

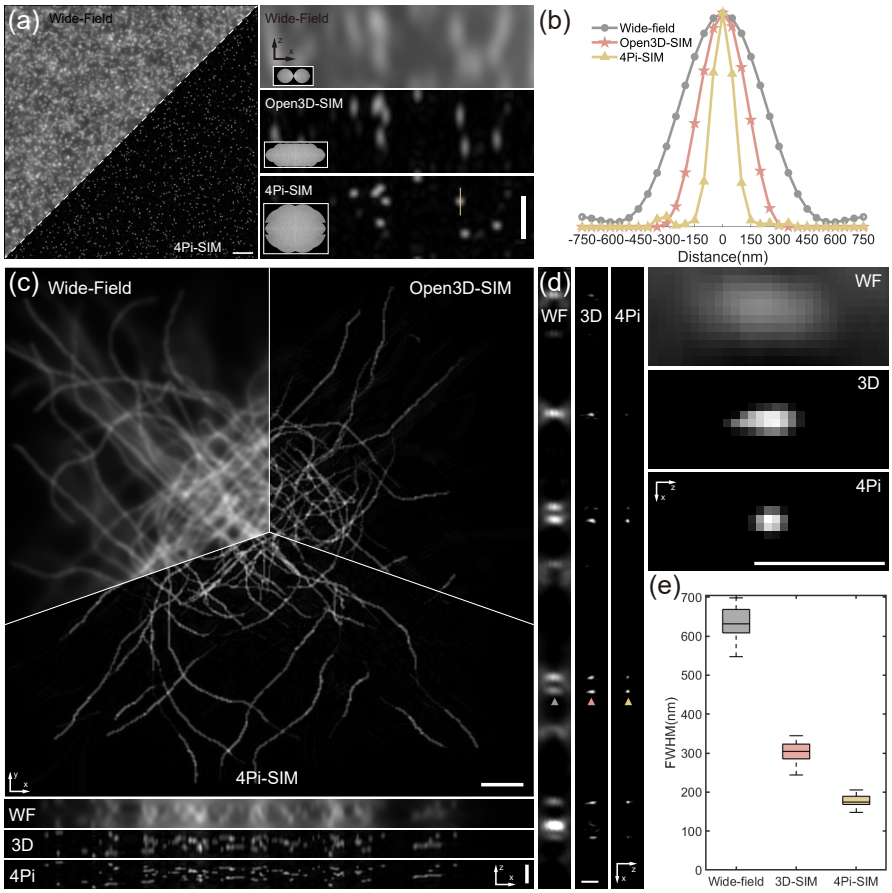

Fig. 2 Simulation and beads experiment. (a)(Left)One layer of simulated beads reconstruction result; (Right)Axial cross-sectional views of simulated beads. Insets show magnitude of OTFs(k_x/k_zplane) derived from images. (b)Line profiles corresponding to bead images shown in the right side of (a), taken along vertical line in (a). (c)Reconstruction results of simulated microtubules, including the comparison of the wide-field, open3D-SIM and our method. (d)(Left)One layer of reconstruction results of 100 nm beads in x-z plane; (Right)Higher magnification views of bead highlighted by colored arrowheads in Left. (e)Quantification of axial FWHM for n = 76, 100 and 100 beads for wide-field microscopy, 3D-SIM and 4Pi-SIM, respectively.Whiskers: maximum and minimum; center lines: medians; bounds of box: 75th and 25th percentiles. Scale bars, 2 μm in(a)(Left), 800 nm in (a)(Right), 2 μm in (c)(Upper), 1 μm in (c)(Lower), 800 nm in (d).

with a spacing of 200 nm can be clearly resolved, underscoring the ability of 4Pi detection to unveil axial detail otherwise masked by diffraction(Fig. 3b).

The effectiveness of the algorithm was also tested. By employing frequency domain filters in the open3D-SIM reconstruction process, side-lobes were surpassed, resulting in structures with crisper edges and enhanced resolution. l_1 norm was used to further mitigate noise and improve the resolution, but it can lead to discontinuities in the structure. The purpose of the frobenius Hessian norm was to correct these discontinuities without losing much resolution, achieving an improvement in image quality

with isotropic properties(Fig. 3c). Profiles perpendicular to the direction of the structure(Fig. 3d1) demonstrate the suppression of noise and the preservation of resolution, while profiles along the direction of the structure(Fig. 3d2) show a smoothing of intensity variations and an enhancement of continuity. By demonstrating several slices in layer stack(Fig. 3e), the orientation and spatial distribution of microtubule growth can be observed.

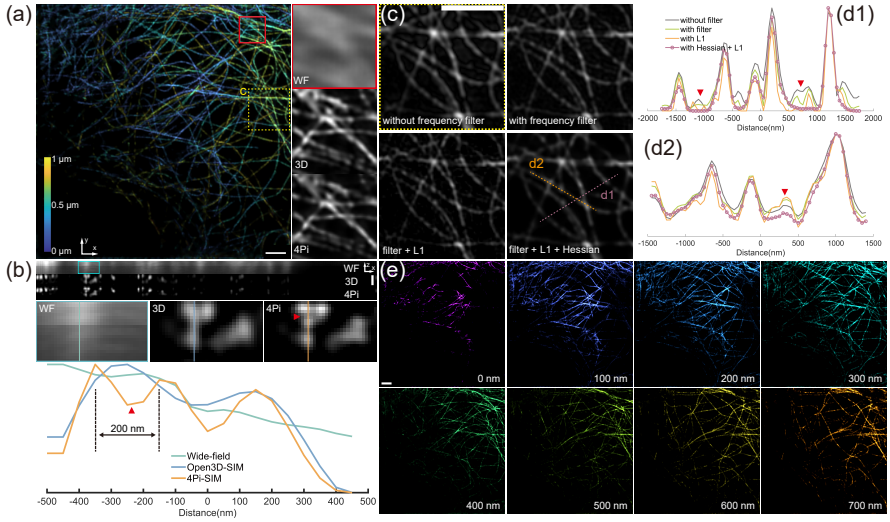

Fig. 3 4Pi-SIM enables near-isotropic imaging of microtubules. (a)(Left)Maximum intensity projection of fixed BSC cells labeled with the Abberior STAR Red. Image is depth coded as indicated; (Right)Higher magnification lateral views(single planes) corresponding to red rectangle in (Left) are shown, comparing wide-field microscopy(upper), 3D-SIM(middle) and 4Pi-SIM(lower). (b)(Top)Axial cross-sectional views of microtubules in (a); (Middle)Higher magnification views corresponding to rectangle indicated in the wide-field (WF) image at the top; (Bottom)Line profiles corresponding to vertical line in the middle view. (c)(Left)Higher magnification lateral views corresponding to yellow dashed rectangle in (a), comparing unmodified image, frequency-filtered image, image modified by frequency filter and sparsity regularization, and image modified by frequency filter and sparsity plus Frobenius Hessian regularization; (Right)Line profiles taken along dashed line d1 and d2 on the Left. (e)Continuous x-y section of the 3D volume from 0 to 700 nm depth with a 100-nm axial interval, illustrating the changing morphology of microtubule networks. Scale bars, 2 μm (a, c, e); 800 nm (b).

Next we tested methods on actin filaments in U2OS in Fig. 4. To more clearly demonstrate, a layer is showcased in which the structures existed densely(Fig. 4a). Here, whether in the y-z view where profiles were perpendicular to the structural direction(Fig. 4b, c), or in the x-z view where profiles were aligned with the structural direction(Fig. 4d, e), the axial resolution was enhanced. It is important to note that when acquiring raw data, only images exhibiting the 4Pi PSF are collected. In our actual optical setup, the fluorescence interference is split into four channels, each corresponding to a specific phase difference (0, $\pi/2$, π, $3\pi/2$ rad). The 3D-SIM reconstruction was performed using the sum of these channels, based on the understanding that the aggregate of four 4Pi PSFs will emulate a wide-field PSF. However, due

to optical aberrations and systematic errors, the four channels cannot be perfectly aligned, leading to a slight tilt in the 3D-SIM outcomes.

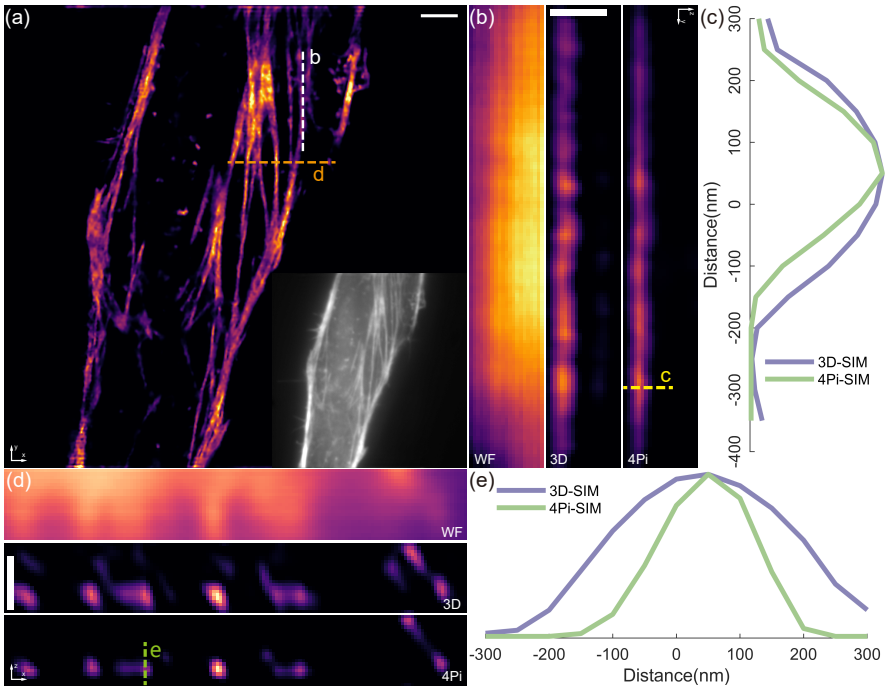

Fig. 4 4Pi-SIM enables the enhancement of axial resolution for actin filaments. (a)Single lateral plane of actin filaments in U2OS labeled with actin-555. (b)Axial views corresponding to white dashed line in (a), comparing wide-field microscopy(WF), 3D-SIM(3D), 4Pi-SIM(4Pi). (c)Line profiles corresponding to yellow dashed line in (b). (d)Axial views corresponding to orange dashed line in (a), comparing wide-field microscopy(WF), 3D-SIM(3D), 4Pi-SIM(4Pi). (e)Line profiles corresponding to green dashed line in (d). Scale bars, 2 μm (a); 80 nm (b,d).

3 Discussion

In order to achieve high-quality imaging, there are several factors that need to be considered: (1)the size of field of view; (2)the aberration correction of system; (3)the selection of reconstruction parameters. As shown in Results section, the field of view(FOV) we used is 25.163 $\mu m \times 25.163$ μm, which only had a pixel size of 301×301. If FOV is expanded, the 4Pi PSF at the periphery of the field will differ from that at the center, because of the varying optical path differences at the edge. This results in the imaging target being only a part of the cell's structure, preventing high-throughput imaging. By introducing vectorial PSF phase retrieval [16, 28] in separate regions, this problem can be improved. Additionally, fluorescent interference is highly sensitive to aberrations, which can lead to the deformation of the PSF and, consequently, distorted results. Here we used adaptive optics, typically deformable mirrors [29], to

address this problem. Although there was still a slight tilt in the PSF, it can have little influence on the quality of the reconstruction.

The selection of reconstruction parameters play a crucial role in the outcome of the reconstruction [30]. For open3D-SIM algorithm, we mainly adjusted the notch depth of $filter_1$ and $filter_2$, to surpass the background noise and at meanwhile maintain signals. With a good outcomes of SIM reconstruction, the following optimization will have a better performance. The parameters in the last step decide whether the optimization can converge and reach the best solution. λ_1 determines the sparsity of the results. The larger its value, the more noise is suppressed, the more discontinuous the structures become, and the sharper the edges are. λ_2 determines the significance of frobenius Hessian norm, enhance the continuity of samples at the sacrifice of resolution. Correct configuration allows for resolution to be maintained or even slightly enhanced when noise and artifacts are mitigated. This needs repeated trials, which is a drawback of the algorithm. For separated samples like beads, λ_1 ought to be large and for continuous samples like microtubules and actin filaments, a larger λ_2 will be appropriate. λ_z controls the importance of axial continuity, most of time it is set to 1 for an isotropic result.

4 Conclusion

In summary, we report 4Pi-SIM, a powerful approach to enhance axial resolution in imaging subcellular structures and morphologies of cells. The method can extend the axial resolution from $\sim 284\ nm$ to $\sim 133\ nm$, about 2-fold improvement, compared with 3D-SIM, and maintain the lateral resolution of 3D-SIM at the same time. Using this approach, the fine axial structures that were difficult to discern in traditional SIM can now be resolved, enhancing the optical sectioning capability.

To overcome the non-uniformity of synthetic OTF in SIM reconstruction, which may cause artifacts and noises, a space-domain optimization was developed based on sparsity(l_1 norm) and continuity(frobenius Hessian norm). They can suppress the background and noise and meanwhile slightly enhance isotropic resolution. By employing the ADMM algorithm for iteration, rapid convergence can be achieved. Our method makes a balance between resolution and acquiring speed, by adding new illumination pattern like 4-beam interference and new algorithm like deep learning, it's limitations can be overcome in the future.

5 Methods

5.1 Details of optimization algorithm

We adopted ADMM to solve the optimization problem in Eq. (1).Scaled ADMM was employed for simplicity. The Augmented Lagrangian function was constructed as:

$$\begin{aligned} L =& \frac{1}{2}\|Hf - b\|_2^2 + \lambda_1\|d_1\|_1 + \\ & \lambda_2\|\sqrt{d_{xx}^2 + d_{xy}^2 + d_{yy}^2 + d_{xz}^2 + d_{yz}^2 + d_{zz}^2}\|_1 + \end{aligned}$$

$$\sum_{\text{for all } d} \left[\frac{\rho}{2}\|Af - d + \omega\|_2^2 - \frac{\rho}{2}\|\omega\|_2^2\right]. \tag{3}$$

For each $d(d_1,\ d_{xx},\ d_{xy},\ d_{yy},\ d_{xz},\ d_{yz},\ d_{zz})$, there is one A operator and one scaled dual variable ω. A is in the form of $I,\ \nabla_{xx},\ \sqrt{2}\nabla_{xy},\ \nabla_{yy},\ \sqrt{2\lambda_z}\nabla_{xz},\ \sqrt{2\lambda_z}\nabla_{yz},\ \lambda_z\nabla_{zz}$, respectively. Here, I denotes an identity matrix of the same size as the input image stack, and operator ∇ represents the second-order partial derivative operation on the image stack indicated by its subscripts.

By minimizing L with respect to f, d, and ω iteratively, the best value of f can be found. Take the partial derivative of L with respect to f and set it equal to zero, we can get:

$$\frac{\partial L}{\partial f} = H^T(Hf - b) + \sum_{\text{for all } d} \left[\rho A^T(Af - d + \omega)\right] = 0. \tag{4}$$

$\cdot^T$ denotes the transpose of a matrix. f can be extracted and solved using the Fourier Transform(Eq. (5)).

$$f^{i+1} = ifftn\left[\frac{\sum_{\text{for all } d} \tilde{A}^* \odot (\tilde{d}^i - \tilde{\omega}^i) + \frac{\tilde{H}^* \odot \tilde{b}}{\rho}}{\sum_{\text{for all } d} |\tilde{A}|^2 + \frac{|\tilde{H}|^2}{\rho}}\right], \tag{5}$$

$\tilde{\cdot}$ is the Fourier Transform of matrix, $\cdot^*$ represents the conjugate of complex matrix, and $\odot$ denotes element-wise multiplication.

Next we update each d through the same way as f, for all d except d_1, the partial derivative of L is calculated(Eq. (6)).

$$\frac{\partial L}{\partial d} = \frac{\lambda_2 d}{\sqrt{d_{xx}^2 + d_{xy}^2 + d_{yy}^2 + d_{xz}^2 + d_{yz}^2 + d_{zz}^2}} + \rho(d - C^i) = 0 \tag{6}$$

$$\begin{cases} C_{xx}^i = \nabla_{xx} f^{i+1} + \omega_{xx}^i \\ C_{xy}^i = \sqrt{2}\nabla_{xy} f^{i+1} + \omega_{xy}^i \\ C_{yy}^i = \nabla_{yy} f^{i+1} + \omega_{yy}^i \\ C_{xz}^i = \sqrt{2\lambda_z}\nabla_{xz} f^{i+1} + \omega_{xz}^i \\ C_{yz}^i = \sqrt{2\lambda_z}\nabla_{yz} f^{i+1} + \omega_{yz}^i \\ C_{zz}^i = \lambda_z \nabla_{zz} f^{i+1} + \omega_{zz}^i \end{cases}$$

Since the d's are coupled, we need to find the multivariate function extremum of L with respect to d. When the six equations derived from Eq. 5 are combined, the following relationships are obtained:

$$\frac{d_{xx}}{C_{xx}} = \frac{d_{xy}}{C_{xy}} = \frac{d_{yy}}{C_{yy}} = \frac{d_{xz}}{C_{xz}} = \frac{d_{yz}}{C_{yz}} = \frac{d_{zz}}{C_{zz}}. \tag{7}$$

Take d_{xx} as example, substituting the above conclusions(Eq. 7) back into Eq. 6, we can obtain:

$$\frac{\lambda_2 d_{xx}}{\sqrt{\sum_{\text{for all } C}\left(\frac{d_{xx}}{C_{xx}}C\right)^2}} + \rho(d_{xx} - C_{xx}) = 0, \tag{8}$$

which can be simplified to:

$$\frac{\lambda_2 \cdot sign(d_{xx})|C_{xx}|}{\sqrt{\sum_{\text{for all } C}(C)^2}} + \rho(d_{xx} - C_{xx}) = 0. \tag{9}$$

Here, $sign(d)$ is 1 when $d > 0$, -1 when $d < 0$, and 0 when $d = 0$. Through classification discussion, the iterative formula for d_{xx} can be summarized as a soft-threshold function:

$$d_{xx}^{i+1} = \begin{cases} C_{xx}^i - |C_{xx}^i|\frac{\lambda_2/\rho}{\sqrt{\sum(C)^2}}, & C_{xx}^i > |C_{xx}^i|\frac{\lambda_2/\rho}{\sqrt{\sum(C)^2}} \\ 0, & -|C_{xx}^i|\frac{\lambda_2/\rho}{\sqrt{\sum(C)^2}} < C_{xx}^i < |C_{xx}^i|\frac{\lambda_2/\rho}{\sqrt{\sum(C)^2}} \\ C_{xx}^i + |C_{xx}^i|\frac{\lambda_2/\rho}{\sqrt{\sum(C)^2}}, & C_{xx}^i < -|C_{xx}^i|\frac{\lambda_2/\rho}{\sqrt{\sum(C)^2}} \end{cases} \tag{10}$$

Similar operations can be applied to the iteration of other d's (except d_1). By considering case when $d = 0$, Eq. 10 can be transformed into a more general form:

$$d_{xx}^{i+1} = max\left(\sqrt{\sum(C^i)^2} - \frac{\lambda_2}{\rho}\right) \odot \frac{C_{xx}^i}{\sqrt{\sum(C^i)^2}}. \tag{11}$$

For d_1, it is easy to derive the iteration formula of d_1, which is also a soft-threshold function:

$$d_1^{i+1} = S_{\frac{\lambda_1}{\rho}}(f^{i+1} + \omega^i), \tag{12}$$

where $S_\gamma(y) = max(y - \gamma, 0) + min(y + \gamma, 0)$. For all ω, the iterations are similar, which can be denoted as:

$$w^{i+1} = w^i + Af^{i+1} - d^{i+1} \tag{13}$$

The pseudo code is as follows:

Algorithm 1 Frobenius Hessian Sparsity Optimization

Input: f^0, H, λ_1, λ_2, λ_z, ρ, IterNum
Output: de-noised image stack f^* with depressed artifacts

```
Initialize:
all d, ω ← f^0.
for i = 0 to IterNum-1 do
    Update f^{i+1} according to Eq. 5.
    Update d_1^{i+1} according to Eq. 12.
    Update d_xx^{i+1}–d_zz^{i+1} according to Eq. 11.
    Update all ω^{i+1} according to Eq. 13.
end for
f* ← f^{IterNum}
```

Acknowledgements. Acknowledgements are not compulsory. Where included they should be brief. Grant or contribution numbers may be acknowledged.

Please refer to Journal-level guidance for any specific requirements.

Funding. This work was financially sponsored by the National Natural Science Foundation of China (62125504, 62361166631); STI 2030—Major Projects (2021ZD0200401); the Fundamental Research Funds for the Central Universities (2022FZZX01-20).

Declarations

Competing interests. The authors declare that they have no competing interests.

References

[1] Hell, S.W., Wichmann, J.: Breaking the diffraction resolution limit by stimulated emission: Stimulated-emission-depletion fluorescence microscopy. Optics Letters **19**(11), 780–782 (1994) https://doi.org/10.1364/OL.19.000780

[2] Wang, W., Li, C., Zhan, Z., Zhang, Z., Han, Y., Kuang, C., Liu, X.: Dual-modulation difference stimulated emission depletion microscopy to suppress the background signal. Advanced Photonics **4**(4), 046001 (2022) https://doi.org/10.1117/1.AP.4.4.046001

[3] Vicidomini, G., Bianchini, P., Diaspro, A.: Sted super-resolved microscopy. Nature Methods **15**(3), 173–182 (2018) https://doi.org/10.1038/nmeth.4593

[4] van de Linde, S., Löschberger, A., Klein, T., Heidbreder, M., Wolter, S., Heilemann, M., Sauer, M.: Direct stochastic optical reconstruction microscopy with

standard fluorescent probes. Nature Protocols **6**(7), 991–1009 (2011) https://doi.org/10.1038/nprot.2011.336

[5] Betzig, E., Patterson, G.H., Sougrat, R., Lindwasser, O.W., Olenych, S., Bonifacino, J.S., *et al.*: Imaging intracellular fluorescent proteins at nanometer resolution. Science **313**(5793), 1642–1645 (2006) https://doi.org/10.1126/science.1127344

[6] Rust, M.J., Bates, M., Zhuang, X.: Sub-diffraction-limit imaging by stochastic optical reconstruction microscopy (storm). Nature Methods **3**(10), 793–796 (2006) https://doi.org/10.1038/nmeth929

[7] Sun, Y., Yin, L., Cai, M., Wu, H., Hao, X., Kuang, C., Liu, X.: Modulated illumination localization microscopy-enabled sub-10 nm resolution. Journal of Innovative Optical Health Sciences **15**(02), 2230004 (2022) https://doi.org/10.1142/S179354582230004X

[8] Gustafsson, M.G.L.: Surpassing the lateral resolution limit by a factor of two using structured illumination microscopy. Journal of Microscopy **198**(2), 82–87 (2000) https://doi.org/10.1046/j.1365-2818.2000.00710.x

[9] Gustafsson, M.G.L., Shao, L., Carlton, P.M., Wang, C.J.R., Golubovskaya, I.N., Cande, W.Z., *et al.*: Three-dimensional resolution doubling in wide-field fluorescence microscopy by structured illumination. Biophysical Journal **94**(12), 4957–4970 (2008) https://doi.org/10.1529/biophysj.107.120345

[10] Shao, L., Kner, P., Rego, E.H., Gustafsson, M.G.L.: Super-resolution 3d microscopy of live whole cells using structured illumination. Nature Methods **8**(12), 1044–1046 (2011) https://doi.org/10.1038/nmeth.1734

[11] Chen, X., Zhong, S., Hou, Y., Cao, R., Wang, W., Li, D., *et al.*: Super-resolution structured illumination microscopy reconstruction algorithms: A review. Light: Science & Applications **12**(1), 172 (2023) https://doi.org/10.1038/s41377-023-01204-4

[12] Han, K.Y., Willig, K.I., Rittweger, E., Jelezko, F., Eggeling, C., Hell, S.W.: Three-dimensional stimulated emission depletion microscopy of nitrogen-vacancy centers in diamond using continuous-wave light. Nano Letters **9**(9), 3323–3329 (2009) https://doi.org/10.1021/nl901597v

[13] Harke, B., Ullal, C.K., Keller, J., Hell, S.W.: Three-dimensional nanoscopy of colloidal crystals. Nano Letters **8**(5), 1309–1313 (2008) https://doi.org/10.1021/nl073164n

[14] Pavani, S.R.P., Thompson, M.A., Biteen, J.S., Lord, S.J., Liu, N., Twieg, R.J., *et al.*: Three-dimensional, single-molecule fluorescence imaging beyond the diffraction limit by using a double-helix point spread function. Proceedings of the

National Academy of Sciences **106**(9), 2995–2999 (2009) https://doi.org/10.1073/pnas.0900245106

[15] Lew, M.D., Lee, S.F., Badieirostami, M., Moerner, W.E.: Corkscrew point spread function for far-field three-dimensional nanoscale localization of pointlike objects. Optics Letters **36**(2), 202–204 (2011) https://doi.org/10.1364/OL.36.000202

[16] Yang, X., Zhu, H., Sun, Y., Wu, H., Han, Y., Hao, X., Kuang, C., Liu, X.: Accurate 3d single-molecule localization via vectorial *in situ* point spread function retrieval and aberration assessment. Photonics Research **12**(11), 2447–2461 (2024) https://doi.org/10.1364/PRJ.520469

[17] Lelek, M., Gyparaki, M.T., Beliu, G., Schueder, F., Griffié, J., Manley, S., *et al.*: Single-molecule localization microscopy. Nature Reviews Methods Primers **1**(1), 1–27 (2021) https://doi.org/10.1038/s43586-021-00038-x

[18] Shao, L., Isaac, B., Uzawa, S., Agard, D.A., Sedat, J.W., Gustafsson, M.G.L.: I5s: Wide-field light microscopy with 100-nm-scale resolution in three dimensions. Biophysical Journal **94**(12), 4971–4983 (2008) https://doi.org/10.1529/biophysj.107.120352

[19] Shao, L., Winoto, L., Agard, D.a., Gustafsson, M.g.l., Sedat, J.w.: Interferometer-based structured-illumination microscopy utilizing complementary phase relationship through constructive and destructive image detection by two cameras. Journal of Microscopy **246**(3), 229–236 (2012) https://doi.org/10.1111/j.1365-2818.2012.03604.x

[20] Li, X., Wu, Y., Su, Y., Rey-Suarez, I., Matthaeus, C., Updegrove, T.B., *et al.*: Three-dimensional structured illumination microscopy with enhanced axial resolution. Nature Biotechnology **41**(9), 1307–1319 (2023) https://doi.org/10.1038/s41587-022-01651-1

[21] Sun, Y., Zhu, H., Yin, L., Wu, H., Cai, M., Sun, W., *et al.*: Fluorescence interference structured illumination microscopy for 3d morphology imaging with high axial resolution. Advanced Photonics **5**(5), 056007 (2023) https://doi.org/10.1117/1.AP.5.5.056007

[22] Gustafsson, Agard, Sedat: I5m: 3d widefield light microscopy with better than 100 nm axial resolution. Journal of Microscopy **195**(1), 10–16 (1999) https://doi.org/10.1046/j.1365-2818.1999.00576.x

[23] Huang, X., Fan, J., Li, L., Liu, H., Wu, R., Wu, Y., *et al.*: Fast, long-term, super-resolution imaging with hessian structured illumination microscopy. Nature Biotechnology **36**(5), 451–459 (2018) https://doi.org/10.1038/nbt.4115

[24] Zhao, W., Zhao, S., Li, L., Huang, X., Xing, S., Zhang, Y., *et al.*: Sparse deconvolution improves the resolution of live-cell super-resolution fluorescence

microscopy. Nature Biotechnology **40**(4), 606–617 (2022) https://doi.org/10.1038/s41587-021-01092-2

[25] Lang, M.C., Staudt, T., Engelhardt, J., Hell, S.W.: 4pi microscopy with negligible sidelobes. New Journal of Physics **10**(4), 043041 (2008) https://doi.org/10.1088/1367-2630/10/4/043041

[26] Cao, R., Li, Y., Chen, X., Ge, X., Li, M., Guan, M., *et al.*: Open-3dsim: An open-source three-dimensional structured illumination microscopy reconstruction platform. Nature Methods **20**(8), 1183–1186 (2023) https://doi.org/10.1038/s41592-023-01958-0

[27] Lefkimmiatis, S., Bourquard, A., Unser, M.: Hessian-based norm regularization for image restoration with biomedical applications. IEEE Transactions on Image Processing **21**(3), 983–995 (2012) https://doi.org/10.1109/TIP.2011.2168232

[28] Thao, N.H., Soloviev, O., Verhaegen, M.: Phase retrieval based on the vectorial model of point spread function. JOSA A **37**(1), 16–26 (2020) https://doi.org/10.1364/JOSAA.37.000016

[29] Huang, F., Sirinakis, G., Allgeyer, E.S., Schroeder, L.K., Duim, W.C., Kromann, E.B., *et al.*: Ultra-high resolution 3d imaging of whole cells. Cell **166**(4), 1028–1040 (2016) https://doi.org/10.1016/j.cell.2016.06.016

[30] Boyd, S.: Distributed optimization and statistical learning via the alternating direction method of multipliers. Foundations and Trends® in Machine Learning **3**(1), 1–122 (2010) https://doi.org/10.1561/2200000016